

Janus-type dual emission of a Cyclometalated Iron(III) complex

Matthias Bauer (✉ matthias.bauer@upb.de)

University of Paderborn <https://orcid.org/0000-0002-9294-6076>

Jakob Steube

University of Paderborn <https://orcid.org/0000-0003-3178-4429>

Ayla Pöpcke

University of Rostock

Olga Bokareva

University of Rostock

Thomas Reuter

Johannes Gutenberg University of Mainz

Serhiy Demeshko

Universität Göttingen

Roland Schoch

University of Paderborn

Stephan Hohloch

University of Paderborn <https://orcid.org/0000-0002-5353-0801>

Franc Meyer

Universität Göttingen <https://orcid.org/0000-0002-8613-7862>

Katja Heinze

Johannes Gutenberg University of Mainz <https://orcid.org/0000-0003-1483-4156>

Oliver Kühn

Institute of Physics, University of Rostock

Stefan Lochbrunner

University of Rostock

Research Article

Keywords: Janus-type dual emission, Cyclometalated Iron(III) complex, Photoactive compounds

Posted Date: September 4th, 2020

DOI: <https://doi.org/10.21203/rs.3.rs-64316/v1>

License:  This work is licensed under a Creative Commons Attribution 4.0 International License.

[Read Full License](#)

Version of Record: A version of this preprint was published at Nature Chemistry on February 27th, 2023.

See the published version at <https://doi.org/10.1038/s41557-023-01137-w>.

Abstract

Photoactive compounds are essential for photocatalytic and luminescent applications, such as photoredox catalysis or light emitting diodes. However, the substitution of noble metals, which are almost exclusively used, by base metals remains a major challenge on the way to a more sustainable world.¹ Iron is a dream candidate for this ambitious aim.² But compared to noble metal complexes that show long-lived metal-to-ligand charge-transfer (MLCT) states, realization of emissive and photoactive iron complexes is demanding, due to the fast deactivation of charge transfer states into non-emissive inactive states. No MLCT emission has been observed for monometallic iron complexes before. Consequently, dual emission could also not yet be realized with iron complexes, as it is a very rare property even of noble metal compounds. Here we report the Fe^{III} complex [Fe(ImP)₂][PF₆] (HImP = 1,1'-(1,3-phenylene)bis(3-methyl-1-imidazol-2-ylidene)), showing Janus-type dual emission by combining LMCT (ligand-to-metal charge transfer) with MLCT luminescence. The respective excited states are characterized by a record lifetime of $\tau_{\text{MLCT}} = 4.2$ ns, and a moderate $\tau_{\text{LMCT}} = 0.2$ ns. Only two emissive Fe^{III} compounds are known so far and they show LMCT luminescence only.^{3,4} The unique properties of the presented complex are caused by the specific ligand design combining four N-heterocyclic carbenes with two cyclometalating groups, using the σ -donor strength of six carbon atoms and the acceptor capabilities of the central phenyl rings. Spectroscopically, doublet manifolds could be identified in the deactivation process, while (TD)DFT analysis revealed the presence of quartets as well. With three key advancements of realizing the first iron complex showing dual luminescence, a MLCT luminescence and a world record MLCT lifetime, the results constitute a basis for future application of iron complexes as white light emitters and new photocatalytic reactions making use of the Janus-type properties of the developed complex.

Main Text

The biggest challenge in the search for photoactive iron complexes¹⁻⁴ is posed by the small ligand field splitting of t_{2g} and e_g^* orbitals, which is smaller in 3d transition metal complexes compared to their 4d and 5d counterparts.⁵ Metal-centered (MC) states typically states act as low-energy “dark” excited state trap, quenching potentially emissive MLCT or LMCT charge-transfer states. Consequently, short lifetimes are observed for CT states.⁶ Attempts to invert the order of MC and CT states focus on the destabilization of MC levels by strong σ -donors,⁷⁻⁹ or the stabilization of CT states by p -acceptors.¹⁰⁻¹³ In Fe^{II} complexes, these strategies lead to MLCT lifetimes in the picosecond range. Exceptionally long MLCT lifetimes could be obtained (i) with six NHC donor groups ($t = 0.5$ ns),¹⁴ and (ii) using the “HOMO-inversion” concept¹⁵ ($t = 2.7$ ns).¹⁶ However, no emissive mononuclear Fe^{II} complexes are known to this date.¹⁷ Contrarily, two emissive Fe^{III} complexes have been reported in the last years. The Fe^{III} congener of the NHC-Fe^{II} complex with 0.5 ns MLCT lifetime presented by Wärnmark *et al.* exhibits the first reported emission from a ²LMCT state with a lifetime of around 100 ps.³ Ligand optimization achieved a value of 2 ns, with a quantum yield of 2 % in aerated solution.⁴ However, no MLCT emission could yet be observed

in Fe^{III} complexes due to the difficult accessibility of iron(IV) in typical coordination complexes. Cyclometalating phenyl-containing ligands offer both strong σ -donor but also π -donor properties which stabilize high oxidation states. Fe^{II} complexes with such ligand types were extensively theoretically by Jakubikova and Dixon.¹⁸⁻²¹ The quantum chemical predictions were recently supported by an experimental study from our groups.²² The Fe^{II} complex, derived from [Fe(tpy)₂]²⁺ (tpy = terpyridin) by exchange of one tpy through a deprotonated phenylbipyridine, showed an extension of the MLCT lifetime by a factor of 5 and a decrease of the MC lifetime. Here we explore the application of cyclometalating ligands in iron(III) complexes to extend CT lifetimes, which finally results in a two-color luminescence that has never been observed for iron complexes before.

The complex [Fe(ImP)₂][PF₆] (HImP = 1,1'-(1,3-phenylene)bis(3-methyl-1-imidazol-2-ylidene)) **1**[PF₆] can be obtained by transmetalation of the C_{NHC}[^]C_{CM}[^]C_{NHC} ligand ImP⁻ (HImP = 1,1'-(1,3-phenylene)bis(3-methyl-imidazole-1-ylidene)) (Fig. 1a),²³⁻²⁵ resulting in a blue air- and water-stable Fe^{III} complex as [PF₆]⁻ salt after workup under atmospheric conditions. The chemical integrity was confirmed by paramagnetic nuclear magnetic resonance (NMR) spectroscopy (Extended Data Fig. 1) and mass spectrometry (Extended Data Fig. 2).

In the crystal structure (Fig. 1b), the C_{NHC}-Fe-C_{NHC} bite angle of 155° is smaller than in the analog terpyridine complex⁸ and leads to a more distorted octahedral geometry. The ligand to ligand dihedral angle is 86°. One counterion is present in the unit cell, in agreement with a Fe^{III} center. The doublet shown in the Mößbauer spectrum of Fig. 1c is characterized by an isomer shift of -0.12 mm s⁻¹ and a quadrupole splitting of 1.59 mm s⁻¹, indicating a d⁵ low-spin complex. Temperature dependent magnetic susceptibility measurements (Extended Data Fig. 3) show the typical behavior of a low-spin Fe^{III} compound, i.e. the $\chi_M T$ values are higher than the spin-only value (0.375 cm³mol⁻¹K vs. 0.49 – 0.64 cm³mol⁻¹K in **1**) and exhibit the expected deviation from the Curie law due to non-quenched orbital momentum of the ²T₂ ground state.

Beyond enforcing a low-spin configuration, the tremendous effect of cyclometalation and the NHC ligands on the electronic structure is revealed by cyclic voltammetry (Fig. 2a). A reversible Fe^{II/III} redox wave is found at very low potential (-1.16 V vs FcH^{0/+}). Compared to the value of 0.31 V for the analogous iron complex with two C[^]N[^]C ligands (2,6-bis(3-methyl-imidazole-1-ylidene)-pyridine), a cathodic shift of 1.47 V is observed.²⁶ This corresponds to the behavior of the [Fe(tpy)₂]²⁺ / [Fe(C[^]N[^]N)(tpy)]⁺ pair with a cathodic shift of 0.83 V.²² A quasi-reversible wave at 0.08 V is assigned to the Fe^{III/IV} couple, while the irreversible wave at E_p = 1.23 V is attributed to ligand oxidation (Extended Data Fig. 4a).

Both MLCT ($\lambda_{\epsilon, \max} = 351$ nm, $\epsilon = 6,000$ M⁻¹ cm⁻¹) and LMCT ($\lambda_{\epsilon, \max} = 585$ nm, $\epsilon = 540$ M⁻¹ cm⁻¹) transitions are observed in the absorption spectrum of **1** (Fig. 2b). Spectra of the electrochemically generated one-electron reduced and oxidized species **1**⁻ and **1**⁺ are shown in Extended Data Fig. 4b. According to DFT calculations, these are metal-centered redox processes, showing the mainly Fe^{II} and Fe^{IV} character of **1**⁻

and 1^+ , respectively (Extended Data Table 1). TDDFT calculations with optimally-tuned range-separated functionals suited for the description of charge-transfer states^{27,28} further reveal the nature of the underlying transitions (Fig. 2b and 2c, Extended data Fig. 5a and 5b). The LMCT absorption is caused by a transition from the ligand π -orbital involving both imidazole and phenyl donors to a singly occupied metal-centered d-acceptor orbital of the t_{2g} set. In the MLCT band, transitions originate from singly and doubly occupied Fe^{III} d-orbitals to the π^* -orbitals of the cyclometalating phenyl ligand. Some transitions in the MLCT region from 300-450 nm are of mixed LMCT/LC character to a certain extent.

Excitation of **1** into the low energy LMCT absorption band at 585 nm results in a broad emission mirroring the LMCT absorption band (Fig. 3a). On the other hand, excitation into the high energy MLCT absorption at 350 nm results in dual room temperature luminescence (Fig. 3a). The high energy emission at $\lambda_{max} = 450$ nm and a broad band emission at $\lambda_{max} = 675$ nm reflect the MLCT and LMCT absorption bands, respectively. From the rather small Stokes shifts, doublet 2MLCT and 2LMCT are deduced as emissive states. The excitation spectra shown in Extended Data Fig. 6a recorded with $\lambda_{em} = 420$ nm and 675 nm largely follow the absorption spectrum, supporting that the observed dual photoluminescence originates from complex **1**. A two-dimensional excitation – emission plot is shown in the Extended Data Fig. 6b. In agreement with the two-color absorption composed of MLCT and LMCT bands, the high energy MLCT emission vanishes with decreasing excitation energy. With decreasing temperature, the emission bands increase in intensity (Extended Data Fig. 7). Dual emission is generally a very rare observation,²⁹ and it is the first time that such a behavior is reported for an iron compound at all. Since luminescent complexes of earth-abundant elements are also still very rare,³⁰ the observation of a Janus-type dual MLCT and LMCT emission is an encouraging development for future substitution of noble by base metals for photochemical applications.

A detailed view on the excited-state landscape of complex **1** is extracted by ultrafast spectroscopy. The transient absorption (TA) spectra after excitation at 330 nm and the decay associated amplitude spectra (DAAS) of a global fit are shown in Fig. 3b. The DAAS are compared to the difference spectra of the reduced $1^- - 1$ and oxidized $1^+ - 1$ species obtained by spectro-electrochemistry (spectra shown in Extended Data Fig. 4b).³¹ The transient spectra are dominated by a strong excited state absorption (ESA) below 550 nm. Towards the red, a second ESA band peaking at 610 nm follows. Three time constants are obtained from the global fit: $t_1 = 0.5 \pm 0.1$ ps, $t_2 = 6 \pm 1$ ps, and $t_3 = 0.24 \pm 0.02$ ns. The slowest component describes the general decay of the ESA features (figure 3b). The strong ESA band in the blue resembles the spectrum of the Fe^{II} species very well, suggesting some LMCT character. Oxidation of the iron(III) center results only in weak absorption changes in the visible domain. Thus, the ESA bands do not feature MLCT character. Accordingly, this time constant is assigned to the 2LMCT state, which decays with a rate of $(0.24 \text{ ns})^{-1}$ back to the ground state. Interestingly, in the blue spectral region of the 0.5 ps component, the DAAS is a mirror image of the LMCT-DAAS. It corresponds therefore to a rise of the dominant ESA band and seems to reflect the population of the LMCT state. The DAAS of the intermediate decay component with a time constant of 6 ps exhibits an ESA band at 420 nm, which does resemble

signatures of neither the Fe^{II} nor Fe^{IV} species. It might be caused by an electronic relaxation from higher lying MLCT states. TA measurements applying pump pulses into the LMCT absorption band at 600 nm, shown in extended data figure 8, reveal the same ESA bands observed at 330 nm excitation but a single exponential signal decay. The time constant is 0.24 ns proving the assignment to an ²LMCT state, which is directly optically excited here.

Streak camera measurements (SCM) with excitation at 330 nm (time resolution 50 ps) reveal a luminescence in the spectral region above 640 nm, reflecting the ²LMCT emission. An additional signal in the spectral range 390 to 600 nm, which extends over a few nanoseconds, corresponds to the luminescence above attributed to the ²MLCT states. A time constant of 0.22 ns is found for the ²LMCT emission, which is in excellent agreement with the TA results. For the ²MLCT luminescence, two time constants of 2.1 ns and 5.2 ns are obtained. The spectrally integrated signal of the ²MLCT emission and the corresponding fit are shown in Fig. 3c. Time correlated single photon counting (TCSPC) experiments verify this result (extended data figure 9), since two decay components with time constants of around 2.1 ns and 9 ns for the ²MLCT emission are obtained. Amplitude spectra for the two decay components, shown in Fig. 3d, were extracted from the SCM data by a global fit. Since the two spectra are basically identical, the two emission components have to originate from the same state. This might indicate that the decay is non-exponential, and the double exponential fit can only approximate the real conditions. It is thus valid to deduce an average MLCT lifetime of 4.2 ns. Speculatively, this effect can be attributed to the flexibility of the ligands which cause a distribution of slightly different conformers. The ²MLCT decay is likely to be sensitive to structure variations in the ensemble of complexes probed.

The spectroscopic results, combined with ground state DFT calculations on the doublet, quartet and sextet state in their respective optimized geometry are summarized in the schematic excited state landscape given in Fig. 4a. Optical excitation in the near UV addresses hot ²MLCT states. Electronic relaxation exhibits a branching shortly after the excitation. The population majority is transferred within 0.5 ps to the lowest ²LMCT state. This state is emissive but decays to the ground state mostly by internal conversion resulting in a lifetime of 0.2 ns. The weak absorption band at 600 nm, associated with the ²LMCT state, shows that the corresponding transition dipole moment is small. In combination with the limited lifetime, a low quantum yield of less than 1 % results, as estimated by the intensity of the solvent Raman bands (Extended Data Fig. 6). A minor fraction of the excited population stays in the MLCT manifold and relaxes to the lowest ²MLCT state. The 6 ps component in the TA measurements can be a signature of this relaxation. The ²MLCT state exhibits a lifetime of 4.2 ns and relaxes non-radiatively as well as radiatively back to the ground state, resulting in the weak but significant MLCT emission in the blue spectral region. The ground state DFT calculations show that a sextet MC state can be most likely excluded from the deactivation pathway since it is strongly destabilized by the tremendous donor properties of the ligands. However, the energy of the ⁴MC state in this approximation is lower than for the ²MLCT and slightly higher than for the ²LMCT. Therefore, ⁴MC states cannot be excluded from

deactivation pathway, although no spectroscopic signature could be detected. But they could act as a quencher for both MLCT and LMCT states and thus explain the observed quantum yield.

The scenario summarized in Fig. 4a is further supported by quantum-chemical TDDFT calculations of potential energy curves, Huang-Rhys factors, and nonadiabatic couplings performed in a constrained way in D_{2d} symmetry (*cf.* Extended Data Fig. 5c). This approach indicates that the description of the dynamics by a few-state scheme is indeed a valuable and easy interpretable simplification, which is already indicated in the TCSPC and SCM discussion. Nevertheless, the qualitative picture derived from the potential energy curves along the symmetric a_1 mode having the strongest Huang-Rhys factor in the given energy range (Fig. 4b) agrees well with the schematics of Fig 4a: A 350 nm excitation prepares a wave packet with contributions from different MLCT and mixed LC/LMCT character states. The many states crossings facilitate the fast 0.5 ps relaxation pathway towards the lower lying 2 LMCT states. Quartet states qualify for participation in this relaxation channel and support the claim for being responsible for the low quantum yield. The second pathway leading to an emissive 2 MLCT state would require a transient structural and electronic stabilization. A possible candidate for such a state has been tentatively assigned in Fig. 4b. Here, already rather small energetic corrections to the potential curves beyond TDDFT and further low symmetry modes, which would in particular stabilize LMCT states, could increase the barrier due to the crossing curves such as to provide a transient trapping of population. Future work has to eliminate the bottlenecks of the limited accuracy of the TDDFT method and identification of the relevant vibrational modes to allow for a quantitative theoretical analysis.

In summary, coordination of phenylene-bis-imidazolyliene ligands to a Fe^{III} center yields an air- and water stable doubly cyclometalated iron complex that shows an unprecedented Janus-type two-color luminescence from both MLCT and LMCT states, respectively. Such a unique behavior originates from the combination of strong NHC and cyclometalating s -donors to cause LMCT luminescence. The additional acceptor-capabilities of the cyclometalating ligand enable the MLCT emission. This is the first time that dual luminescence is reported for an iron complex, but also MLCT emission has not been observed for mono-nuclear iron compounds before.¹⁷ While the LMCT state already has a considerable lifetime of 0.2 ns, the MLCT state shows an even longer lifetime of 4.2 ns, which is the longest measured CT lifetime for iron complexes so far. With these results, the foundations for the usage of earth-abundant iron and its complexes in numerous photochemical and photophysical applications are set. Based on the presented data, iron-based white light emitters and multifunctional photoredox catalysts become accessible.

Declarations

J.S. thanks the German Federal Environmental Foundation (Deutsche Bundesstiftung Umwelt - DBU) for a PhD scholarship. This work was performed in the framework of the SPP 2102 funded by the Deutsche Forschungsgemeinschaft (BA 4467/7-1, HE 2778/14-1, KU 952/12-1, LO 714/11-1, ME 1313/15-1).

Author contributions

J.S. carried out the synthesis of the title molecule, provided and analyzed NMR, MS, Cyclic and Square Wave Voltammetry, optical absorption and initial emission spectroscopy, performed Time Correlated Single Photon Counting Spectroscopy and wrote the manuscript. A.P. and S.L. recorded and analyzed emission, transient absorption, and streak camera measurements, analyzed Time Correlated Single Photon Counting Spectroscopy and wrote the manuscript. O.B and O.K. performed and analyzed DFT and TDDFT calculations and wrote the manuscript. T.R. and K.H. performed and analyzed spectro-electrochemical measurements, variable-temperature emission and EPR spectroscopy and wrote the manuscript. S.H. and R.S. performed Single crystal structure. R.S. wrote the manuscript. S.D. and F.M. recorded and analyzed the SQUID and ^{57}Fe Mößbauer data. Principal investigator M.B. conceived and planned the research, contributed to the design of the title molecule, and wrote the manuscript.

Author Information

The authors declare no competing financial interest. Correspondence and material requests should be addressed to M.B. (matthias.bauer@upb.de)

References

1. Larsen, C. B. & Wenger, O. S. Photoredox Catalysis with Metal Complexes Made from Earth-Abundant Elements. *Chem. Eur. J.* **24**, 2039–2058; 10.1002/chem.201703602 (2018).
2. Wenger, O. S. Is Iron the New Ruthenium? *Chem. Eur. J.* **25**, 6043–6052; 10.1002/chem.201806148 (2019).
3. Chabera, P. *et al.* A low-spin Fe(III) complex with 100-ps ligand-to-metal charge transfer photoluminescence. *Nature* **543**, 695–699; 10.1038/nature21430 (2017).
4. Kjær, K. S. *et al.* Luminescence and reactivity of a charge-transfer excited iron complex with nanosecond lifetime. *Science* **363**, 249–253; 10.1126/science.aau7160 (2019).
5. McCusker, J. K. Electronic structure in the transition metal block and its implications for light harvesting. *Science* **363**, 484–488; 10.1126/science.aav9104 (2019).
6. Monat, J. E. & McCusker, J. K. Femtosecond Excited-State Dynamics of an Iron(II) Polypyridyl Solar Cell Sensitizer Model. *J. Am. Chem. Soc.* **122**, 4092–4097; 10.1021/ja992436o (2000).
7. Liu, Y., Persson, P., Sundstrom, V. & Wärnmark, K. Fe N-Heterocyclic Carbene Complexes as Promising Photosensitizers. *Acc. Chem. Res.* **49**, 1477–1485; 10.1021/acs.accounts.6b00186 (2016).
8. Zimmer, P. *et al.* The Connection between NHC Ligand Count and Photophysical Properties in Fe(II) Photosensitizers. An Experimental Study. *Inorg. Chem.* **57**, 360–373; 10.1021/acs.inorgchem.7b02624 (2018).
9. Zimmer, P. *et al.* Towards Noble-Metal-Free Dyads: Ground and Excited State Tuning by a Cobalt Dimethylglyoxime Motif Connected to an Iron N-Heterocyclic Carbene Photosensitizer. *Eur. J. Inorg. Chem.* **2018**, 5203–5214; 10.1002/ejic.201800946 (2018).

10. Liu, L. *et al.* A new record excited state (3)MLCT lifetime for metalorganic iron(ii) complexes. *Phys. Chem. Chem. Phys.* **18**, 12550–12556; 10.1039/c6cp01418f (2016).
11. Darari, M. *et al.* Iron(ii) complexes with diazanyl-NHC ligands: impact of π -deficiency of the azine core on photophysical properties. *Dalton. Trans.* **48**, 10915–10926; 10.1039/c9dt01731c (2019).
12. Jamula, L. L., Brown, A. M., Guo, D. & McCusker, J. K. Synthesis and characterization of a high-symmetry ferrous polypyridyl complex. Approaching the 5T₂/3T₁ crossing point for Fe(II.). *Inorg. Chem.* **53**, 15–17; 10.1021/ic402407k (2014).
13. Mengel, A. K. C. *et al.* A heteroleptic push-pull substituted iron(II) bis(tridentate) complex with low-energy charge-transfer states. *Chem. Eur. J.* **21**, 704–714; 10.1002/chem.201404955 (2015).
14. Chabera, P. *et al.* A FeII Hexa N-Heterocyclic Carbene Complex with a 528 ps Metal-to-Ligand Charge-Transfer Excited-State Lifetime. *J. Phys. Chem. Lett.* **9**, 459–463; 10.1021/acs.jpcclett.7b02962 (2018).
15. Mukherjee, S., Torres, D. E. & Jakubikova, E. HOMO inversion as a strategy for improving the light-absorption properties of Fe(ii) chromophores. *Chem. Sci.* **8**, 8115–8126; 10.1039/c7sc02926h (2017).
16. Jason D. Braun *et al.* Iron(ii) coordination complexes with panchromatic absorption and nanosecond charge-transfer excited state lifetimes. *Nat. Chem.* **11**, 1144–1150; 10.1038/s41557-019-0357-z (2019).
17. Jiang, T. *et al.* Electronic structure and photophysics of a supermolecular iron complex having a long MLCT-state lifetime and panchromatic absorption. *Proc Natl Acad Sci USA*; 10.1073/pnas.2009996117 (2020).
18. Bowman, D. N., Bondarev, A., Mukherjee, S. & Jakubikova, E. Tuning the Electronic Structure of Fe(II) Polypyridines via Donor Atom and Ligand Scaffold Modifications. A Computational Study. *Inorg. Chem.* **54**, 8786–8793; 10.1021/acs.inorgchem.5b01409 (2015).
19. Mukherjee, S., Bowman, D. N. & Jakubikova, E. Cyclometalated Fe(II) complexes as sensitizers in dye-sensitized solar cells. *Inorg. Chem.* **54**, 560–569; 10.1021/ic502438g (2015).
20. Dixon, I. M., Khan, S., Alary, F., Boggio-Pasqua, M. & Heully, J.-L. Probing the photophysical capability of mono and bis(cyclometallated) Fe(ii) polypyridine complexes using inexpensive ground state DFT. *Dalton. Trans.* **43**, 15898–15905; 10.1039/c4dt01939c (2014).
21. Dixon, I. M., Alary, F., Boggio-Pasqua, M. & Heully, J.-L. Reversing the relative (3)MLCT-(3)MC order in Fe(ii) complexes using cyclometallating ligands: a computational study aiming at luminescent Fe(ii) complexes. *Dalton. Trans.* **44**, 13498–13503; 10.1039/c5dt01214g (2015).
22. Steube, J. *et al.* Excited-State Kinetics of an Air-Stable Cyclometalated Iron(II) Complex. *Chem. Eur. J.* **25**, 11826–11830; 10.1002/chem.201902488 (2019).
23. Reilly, S. W., Webster, C. E., Hollis, T. K. & Valle, H. U. Transmetalation from CCC-NHC pincer Zr complexes in the synthesis of air-stable CCC-NHC pincer Co(iii) complexes and initial hydroboration trials. *Dalton. Trans.* **45**, 2823–2828; 10.1039/c5dt04752h (2016).

24. Hollis, T. K. & Webster, C. E. *Unsymmetrical Salts, CCC-NHC Pincer Metal Complexes and Methods of Making the Same. International Patent* (2018), B01J31/02; B01J31/16; B01J31/18; C07D235/02; C07D235/04; C07D235/08, https://worldwide.espacenet.com/publicationDetails/biblio?FT=D&date=20180927&DB=&locale=en_EP&CC=WO&NR=2018175659A1&KC=A1&ND=5.
25. Rubio, R. J. *et al.* Toward a general method for CCC N-heterocyclic carbene pincer synthesis: Metallation and transmetallation strategies for concurrent activation of three C–H bonds. *J. Organomet. Chem.* **690**, 5353–5364; 10.1016/j.jorganchem.2005.05.007 (2005).
26. Liu, Y. *et al.* Towards longer-lived metal-to-ligand charge transfer states of iron(II) complexes: an N-heterocyclic carbene approach. *Chem. Comm.* **49**, 6412–6414; 10.1039/C3CC43833C (2013).
27. Bokareva, O. S., Grell, G., Bokarev, S. I. & Kühn, O. Tuning Range-Separated Density Functional Theory for Photocatalytic Water Splitting Systems. *J. Chem. Theory Comput.* **11**, 1700–1709; 10.1021/acs.jctc.5b00068 (2015).
28. Möhle, T., Bokareva, O. S., Grell, G., Kühn, O. & Bokarev, S. I. Tuned Range-Separated Density Functional Theory and Dyson Orbital Formalism for Photoelectron Spectra. *J. Chem. Theory Comput.* **14**, 5870–5880; 10.1021/acs.jctc.8b00707 (2018).
29. Dorn, M. *et al.* A Vanadium(III) Complex with Blue and NIR-II Spin-Flip Luminescence in Solution. *J. Am. Chem. Soc.* **142**, 7947–7955; 10.1021/jacs.0c02122 (2020).
30. Förster, C. & Heinze, K. Photophysics and photochemistry with Earth-abundant metals - fundamentals and concepts. *Chem. Soc. Rev.* **49**, 1057–1070; 10.1039/c9cs00573k (2020).
31. Brown, A. M., McCusker, C. E. & McCusker, J. K. Spectroelectrochemical identification of charge-transfer excited states in transition metal-based polypyridyl complexes. *Dalton. Trans.* **43**, 17635–17646; 10.1039/c4dt02849j (2014).

Methods

Synthesis.

Dry THF was obtained from an MBraun SPS-800 solvent drying system and was subsequently stored over 4 Å molecular sieve. ¹H NMR spectra were recorded using a Bruker Avance 500 spectrometer. Chemical shifts are calibrated to the residual solvent. ESI-MS spectra were recorded with a Waters Synapt G2 quadrupole – Time of Flight spectrometer. Iron(II) bromide (99.8 %) was purchased from Sigma Aldrich, tetrakis(dimethylamino)zirconium from abcr. 1,1'-(1,3-Phenylene)bis(3-methyl-1-imidazolium) diiodide was synthesized based on literature methods.¹ The synthesis of bis(2,6-bis(3-methylimidazol-1-ylidene)phenyl)iron(III) hexafluorophosphate ([Fe(ImP)₂][PF₆]) is based on a modified literature synthesis.^{2,3} 1,1'-(1,3-Phenylene)bis(3-methyl-1-imidazolium) diiodide (1976 mg, 4 mmol) and tetrakis(dimethylamino)zirconium (1124 mg, 4.2 mmol) were suspended in dry THF (20 mL) in a glovebox. The yellow suspension was stirred for 2 h, then iron(II) bromide (432 mg, 2 mmol) was added. The mixture stirred for another 16 h. The red/orange mixture was worked up under laboratory atmosphere and methanol (2 mL) was added. The now blue suspension was stirred under atmosphere for 1 h, until no

further precipitation of a pale solid was observed. The suspension was filtered through a cotton ball and afterwards through a porous glass frit. The respective filter cakes were washed with acetonitrile until the filtrate turned colorless. The solvent of the filtrate was evaporated using a rotary evaporator. The blue solid was dissolved in dichloromethane and filtered over a silica column. The column was washed thoroughly with dichloromethane. The blue band was eluted with acetonitrile. The solvent of the blue fraction was evaporated. The solid was dissolved in methanol and KPF_6 (2 eq., 736 mg, 4 mmol) were added. The desired compound **1** was precipitated by the addition of water and filtered off. It was redissolved in methanol and treated again with KPF_6 (2 eq) and precipitated again with water to ensure full replacement of the counterion. The suspension was filtered, and the blue solid was dried thoroughly under vacuum. It was then dissolved in a minimal amount of dichloromethane and pentane was allowed to diffuse into the solution. Dark blue long needles of **1**[PF_6] were obtained (415 mg, 0.62 mmol, 31 %) after crystallization overnight which were dried in a vacuum (10^{-3} mbar) for 6 h prior to elemental analysis and spectroscopic measurements. $^1\text{H NMR}$ (500 MHz, CD_3CN) δ (ppm) = 24.70 (4H), 9.68 (12 H), 2.90 (4H), -2.39 (4H), -35.79 (2H; **ESI-MS**: Calculated for [**1**- PF_6] $^+$ ($\text{C}_{28}\text{H}_{26}\text{FeN}_8$) 530.1625, found 530.1621; **Infrared (ATR)**: 3166 cm^{-1} , 3141 cm^{-1} , 2926 cm^{-1} , 1587 cm^{-1} , 1470 cm^{-1} , 1455 cm^{-1} , 1405 cm^{-1} , 1344 cm^{-1} , 1263 cm^{-1} , 1232 cm^{-1} , 1075 cm^{-1} , 874 cm^{-1} , 824 cm^{-1} , 769 cm^{-1} , 714 cm^{-1} , 682 cm^{-1} , 555 cm^{-1} , 394 cm^{-1} , 354 cm^{-1} , 258 cm^{-1} **Elemental Analysis** for $\text{C}_{28}\text{H}_{26}\text{F}_6\text{FeN}_8\text{P}$ (Calculated, Found (%)): C (49.80, 49.76), H (3.88, 4.25), N (16.59, 16.30).

X-ray diffraction analysis.

The single crystal data were recorded using a Bruker SMART CCD area-detector diffractometer equipped with a graphite monochromator. The measurements were carried out using Mo K α radiation ($\lambda = 1.54178\text{ \AA}$) at $T = 200(2)\text{ K}$, since at lower temperatures a phase transition occurred, which caused a vaguer diffraction pattern. Structure solution was carried out by direct methods⁴ and structure refinement was conducted using full-matrix least squares refinement based on F^2 .⁴ All non-H-atoms were refined anisotropically and the hydrogen atom positions were derived from geometrical reasons – except hydrogens of methyl groups. They were located from Fourier map using HFIX 137 by SHELX.⁴ All hydrogen atoms were refined at idealized positions riding on the carbon atoms with isotropic displacement parameters $U_{\text{iso}}(\text{H}) = 1.2U_{\text{eq}}(\text{C})$ resp. $1.5U_{\text{eq}}(-\text{CH}_3)$ and C-H bond lengths of 0.93-0.96 \AA . All CH_3 hydrogen atoms were allowed to rotate but not to tip. One dichloromethane solvent molecule could not be modelled during refinement and was treated using SQUEEZE from the platon software package.⁵⁻⁷

($\text{C}_{28}\text{H}_{26}\text{N}_8\text{Fe}$)(PF_6), $M_r = 675.40\text{ Da}$, purple block, size $0.42 \times 0.37 \times 0.25\text{ mm}^3$, monoclinic space group $P2_1/c$ with $Z=4$, $a = 13.6367(12)\text{ \AA}$, $b = 8.7801(8)\text{ \AA}$, $c = 27.099(3)\text{ \AA}$, $\beta = 96.285(2)^\circ$, $V = 3225.2(5)\text{ \AA}^3$, $D_c = 1.391\text{ mg/m}^3$, $\mu = 0.583\text{ mm}^{-1}$, $F(000) = 1380$, $\theta_{\text{max}} = 26.462^\circ$, reflections collected: 28802, independent reflections: 6622, $R_{\text{int}} = 0.0455$, refinement converged at $R1 = 0.0571$ [$I > 2\sigma(I)$], $wR2 = 0.1683$ [all data], min./max. ΔF : -0.578 e\AA^{-3} (0.61 \AA from F123) / 0.804 e\AA^{-3} (0.62 \AA from F123)

Crystallographic data deposition.

Crystallographic data have been deposited at the Cambridge Crystallographic Data Centre assigned to the deposition number CCDC 2002774. Copies are available free of charge via www.ccdc.cam.ac.uk.

Möbßbauer spectroscopy. Möbßbauer spectra were recorded with a ^{57}Co source in a Rh matrix using an alternating constant acceleration *Wissel* Mössbauer spectrometer operated in the transmission mode and equipped with a *Janis* closed-cycle helium cryostat. Isomer shifts are given relative to iron metal at ambient temperature. Simulation of the experimental data was performed with the *Mfit* program using *Lorentzian* line doublets: E. Bill, Max-Planck Institute for Chemical Energy Conversion, Mülheim/Ruhr, Germany.

Magnetic susceptibility measurements. Temperature-dependent magnetic susceptibility measurements were carried out with a *Quantum-Design* MPMS3 SQUID magnetometer in the range from 300 to 2.0 K at a magnetic field of 0.5 T. The powdered sample was contained in a polycarbonate capsule and fixed in a non-magnetic sample holder. Each raw data file for the measured magnetic moment was corrected for the diamagnetic contribution of the sample holder and the capsule. The molar susceptibility data were corrected for the diamagnetic contribution.

Cyclic voltammetry and square wave voltammetry.

Dry acetonitrile was obtained by passing HPLC grade acetonitrile (fisher) over a column of MP Biomedicals MP Alumina N-Super I which was activated in an oven at 150 °C for multiple days. The cyclic and square wave voltammetry measurements were performed at room temperature in 0.1 M $[(n\text{Bu}_4\text{N})[\text{PF}_6]]$ dry acetonitrile solution with an analyte concentration of 0.001 M under a solvent-saturated Argon atmosphere. A three electrode arrangement with a 1 mm Pt working electrode and Pt-wire counter electrode (both Metrohm) and an Ag/AgCl reference electrode (custom built) was used, with the PGSTAT101 potentiostat from Metrohm. Ferrocene was added after the measurements as an internal standard, all potentials were referenced against the $\text{FcH}^{0/+}$ couple. The voltammograms were analyzed using the NOVA software (version 2.1.3), diagnostic criteria for reversibility are based on those proposed by Nicholson^{8,9} and the Randles-Sevcik^{10,11} equation.

Spectroelectrochemistry.

UV/Vis/NIR spectroelectrochemical experiments were performed using a BioLogic SP-50 voltammetric analyzer and a Specac omni-cell liquid transmission cell with CaF_2 windows equipped with a Pt-gauze working electrode, a Pt-gauze counter electrode and a Ag wire as pseudo reference electrode, melt-sealed in a polyethylene spacer (approximate path length 1mm) in CH_3CN containing 0.1 M $[(n\text{Bu}_4\text{N})[\text{PF}_6]]$.¹²

Absorption spectroscopy (steady state).

Acetonitrile of spectroscopic grade (Spectronorm VWR Acetonitrile) was used as solvent for steady-state absorption spectroscopy.

Steady state absorption spectra were recorded using solutions with concentrations of about 10^{-5} M in quartz-cuvettes (pathlength 10 mm) by a Cary 50 spectrometer.

Room temperature emission spectroscopy.

For steady-state emission spectroscopy acetonitrile of spectroscopic grade was used as solvent.

Steady-state emission spectra were recorded in 10 mm quartz cuvettes on a Jasco FP8300 or a Horiba Scientific FluoroMax-4 spectrometer. The solutions for the measurements under argon were degassed via the freeze-pump-thaw technique.

Variable temperature emission spectroscopy.

Variable-Temperature Emission spectra were recorded on a Varian Cary Eclipse spectrometer. For low temperature photoluminescence measurements, a solution of the complex in butyronitrile (refluxed over Na_2CO_3 and KMnO_4 , distilled and stored over aluminium oxide) was filled into a quartz cuvette in an argon-filled glovebox and the cuvette was sealed and transferred to an Oxford cryostate (Oxford instruments Opti-stat^{DN}). Measurements were conducted between 295 K and 77 K.

Time Correlated Single Photon Counting and Time Resolved Emission Spectroscopy.

Time Resolved Emission Spectroscopy (TRES) was performed by time correlated single photon counting (TCSPC) using a Horiba Ultima-01-DD system (Horiba Jobin Yvon GmbH). The degassed sample solution was excited at 346 nm using a Horiba DD350 pulsed LED with a maximum repetition rate of 20 MHz. The emission was recorded in 5 nm steps between 380 and 490 nm for 1 h per wavelength in reverse mode with a slit of 6 nm of the emission monochromator. Excitation at 374 nm was performed with a Horiba DD375L laser diode with a maximum repetition rate of 100 MHz, the emission was recorded in 5 nm steps between 390 and 455 nm in reverse mode with a slit of 6 nm of the emission monochromator. Repetitive start-stop signals were recorded by a multi-channel analyzer over the course of 1 h per wavelength. A histogram of photons was recorded as a function of 16383 channels on a time-range of 100 ns (0.012 ns per channel). To evaluate the TRES data, a global fitting procedure was applied to the data, similar to the analysis of the transient absorption data.

Femtosecond Transient Absorption Spectroscopy.

Femtosecond transient absorption spectra were recorded using excitation wavelengths in three different optical regions and thereby somewhat different pump-probe setups. In all cases they are based on regenerative Ti:sapphire laser systems operating at a frequency of 1 kHz and at a center wavelength of 775 nm (CPA 2001, Clark MXR, Inc.) respectively 800 nm (Spitfire Pro, Spectra-Physics). For probing, a white light continuum generated by focusing a small fraction of the Ti:sapphire output into a CaF_2 crystal

was used. Pump and probe beam were focused onto the sample to overlapping spots with diameters in the range of 200 to 400 μm for the pump and of 100 μm for the probe. The polarizations of the pump and probe pulses were set to magic angle with respect to each other. After the sample, the probe was dispersed by a prism and transient absorption changes were spectrally resolved recorded by an array detector.

For pumping the sample with an excitation wavelength of 400 nm the output of the Ti:sapphire system (Spitfire Pro) was frequency doubled by a BBO crystal. The resulting time resolution was about 150 fs.

To obtain ultrashort excitation pulses in the visible with a center wavelength of 600 nm a non-collinear optical parametric amplifier (NOPA) pumped by the Ti:sapphire system (CPA 2001) was applied. The dispersion of the NOPA pulses was minimized by a compressor based on fused silica prisms resulting in an overall time resolution of better than 100 fs.

For excitation in the UV, i. e., at a center wavelength of 330 nm, the NOPA was tuned to 660 nm and its output was frequency doubled by 100 μm thick BBO crystal cut for type I phase matching.

For all measurements, the iron complex was dissolved in acetonitrile under argon and the sample solution was filled into a fused silica cuvette with a thickness of 1 mm.

The obtained data was fitted using a global fit. In the global fit, the multi-exponential model function, convoluted with the temporal response of the pump-probe setup, is fitted to the complete set of time dependent transient absorption spectra. In the present case three exponential decay components were necessary to reproduce the data with satisfying accuracy, i. e. $N = 3$

Streak Camera Measurements.

In addition to the TCSPC measurements, the time resolved luminescence was also investigated applying a streak camera (Streakscope C10627, Hamamatsu Photonics). The samples were prepared and measured under argon in 1 cm cuvettes. For excitation at 330 nm, a NOPA pumped by a Ti:sapphire laser system (CPA 2001, Clark MXR, Inc.) was set to a center wavelength of 660 nm and its output pulses were frequency doubled by a BBO crystal. To ensure that only radiation at 330 nm reaches the sample, a fused silica prism was applied to separate the UV pulses from the fundamental.

The luminescence lifetimes were determined by fitting a monoexponential decay to the data in the spectral region 640 to 840 nm and a double exponential decay to the data of the region 390 to 600 nm.

Theoretical Calculations.

Quantum-chemical calculations were performed at D_{2d} symmetry with DFT and linear response TDDFT using the optimally-tuned long-range separation functional LC-BLYP together with combined basis set: def2TZVP (Fe) and 6-311G(d,p) (all other atoms). Tuning of the functional was done with the so-called ΔSCF method¹³⁻¹⁵, the details can be found in the work of Bokarev *et al.*¹⁶ The following parameters

were obtained for the present complex: $\alpha=0.0$ (percentage of exact exchange in short-range) and 0.15 bohr^{-1} (long-range separation parameter). Solvent effects (acetonitrile) were taken into account within the polarized continuum model (PCM) approach.¹⁷ Calculations were done with G16¹⁸ and the Q-Chem 5.3¹⁹ packages. Excited state analysis was performed using the TheoDORE package.²⁰ Analysis of Huang-Rhys factors, tuning of functional, and generation of geometries along normal modes were done with in-house codes.

Data Availability

The data generated and analyzed during the current study are available from the corresponding author on reasonable request. X-ray source data for fig. 1b are deposited under CCDC identifier CCDC 2002774 and are available in the supporting information.

Code Availability

The code used for analysis of Huang-Rhys factors, tuning of functional, and generation of geometries along normal modes is available from O.K. upon reasonable request.

Methods References

1. Collado, A. *et al.* Synthesis of Au I - and Au III -Bis(NHC) Complexes: Ligand Influence on Oxidative Addition to Au I Species. *Eur. J. Inorg. Chem.* **2016**, 4111–4122; 10.1002/ejic.201600791 (2016).
2. Reilly, S. W., Webster, C. E., Hollis, T. K. & Valle, H. U. Transmetalation from CCC-NHC pincer Zr complexes in the synthesis of air-stable CCC-NHC pincer Co(iii) complexes and initial hydroboration trials. *Dalton. Trans.* **45**, 2823–2828; 10.1039/c5dt04752h (2016).
3. Hollis, T. K. & Webster, C. E. *Unsymmetrical Salts, CCC-NHC Pincer Metal Complexes and Methods of Making the Same. International Patent* (2018), B01J31/02; B01J31/16; B01J31/18; C07D235/02; C07D235/04; C07D235/08, https://worldwide.espacenet.com/publicationDetails/biblio?FT=D&date=20180927&DB=&locale=en_EP&CC=WO&NR=2018175659A1&KC=A1&ND=5.
4. Sheldrick, G. M. A short history of SHELX. *Acta Crystallogr., Sect. A: Found. Crystallogr.* **64**, 112–122; 10.1107/S0108767307043930 (2008).
5. Spek, A. L. Structure validation in chemical crystallography. *Acta Crystallogr. D* **65**, 148–155; 10.1107/S090744490804362X (2009).
6. Spek, A. L. *PLATON - A Multipurpose Crystallographic Tool* (Utrecht University, Utrecht, 2011).
7. Spek, A. L. PLATON SQUEEZE: a tool for the calculation of the disordered solvent contribution to the calculated structure factors. *Acta crystallographica. Section C, Structural chemistry* **71**, 9–18; 10.1107/S2053229614024929 (2015).
8. Nicholson, R. S. & Shain, I. Theory of Stationary Electrode Polarography. Single Scan and Cyclic Methods Applied to Reversible, Irreversible, and Kinetic Systems. *Anal. Chem.* **36**, 706–723; 10.1021/ac60210a007 (1964).

9. Heinze, J. Cyclic Voltammetry - "Electrochemical Spectroscopy". *New Analytical Methods*(25). *Angew. Chem. Int. Ed. Engl.* **23**, 831–847; 10.1002/anie.198408313 (1984).
10. Randles, J. E. B. A cathode ray polarograph. Part II.—The current-voltage curves. *Trans. Faraday Soc.* **44**, 327–338; 10.1039/TF9484400327 (1948).
11. Scholz, F. *et al. Electroanalytical Methods* (Springer Berlin Heidelberg, Berlin, Heidelberg, 2010).
12. Krejčík, M., Daněk, M. & Hartl, F. Simple construction of an infrared optically transparent thin-layer electrochemical cell. *J. Electroanal. Chem. Interf. Electrochem.* **317**, 179–187; 10.1016/0022-0728(91)85012-E (1991).
13. Livshits, E. & Baer, R. A well-tempered density functional theory of electrons in molecules. *Phys. Chem. Chem. Phys.* **9**, 2932–2941; 10.1039/B617919C (2007).
14. Stein, T., Kronik, L. & Baer, R. Reliable prediction of charge transfer excitations in molecular complexes using time-dependent density functional theory. *J. Am. Chem. Soc.* **131**, 2818–2820; 10.1021/ja8087482 (2009).
15. Stein, T., Kronik, L. & Baer, R. Prediction of charge-transfer excitations in coumarin-based dyes using a range-separated functional tuned from first principles. *J. Chem. Phys.* **131**, 244119; 10.1063/1.3269029 (2009).
16. Möhle, T., Bokareva, O. S., Grell, G., Kühn, O. & Bokarev, S. I. Tuned Range-Separated Density Functional Theory and Dyson Orbital Formalism for Photoelectron Spectra. *J. Chem. Theory Comput.* **14**, 5870–5880; 10.1021/acs.jctc.8b00707 (2018).
17. Tomasi, J., Mennucci, B. & Cammi, R. Quantum mechanical continuum solvation models. *Chem. Rev.* **105**, 2999–3093; 10.1021/cr9904009 (2005).
18. Frisch, M. J. *et al. Gaussian 16 Rev. C.01* (Wallingford, CT, 2016).
19. Shao, Y. *et al.* Advances in molecular quantum chemistry contained in the Q-Chem 4 program package. *Mol. Phys.* **113**, 184–215; 10.1080/00268976.2014.952696 (2015).
20. Plasser, F. TheoDORE: A toolbox for a detailed and automated analysis of electronic excited state computations. *J. Chem. Phys.* **152**, 84108; 10.1063/1.5143076 (2020).

Supplementary Information

Supplementary Information, consisting of SXR D Data and coordinates of the optimized structures, is available for this paper.

Figures

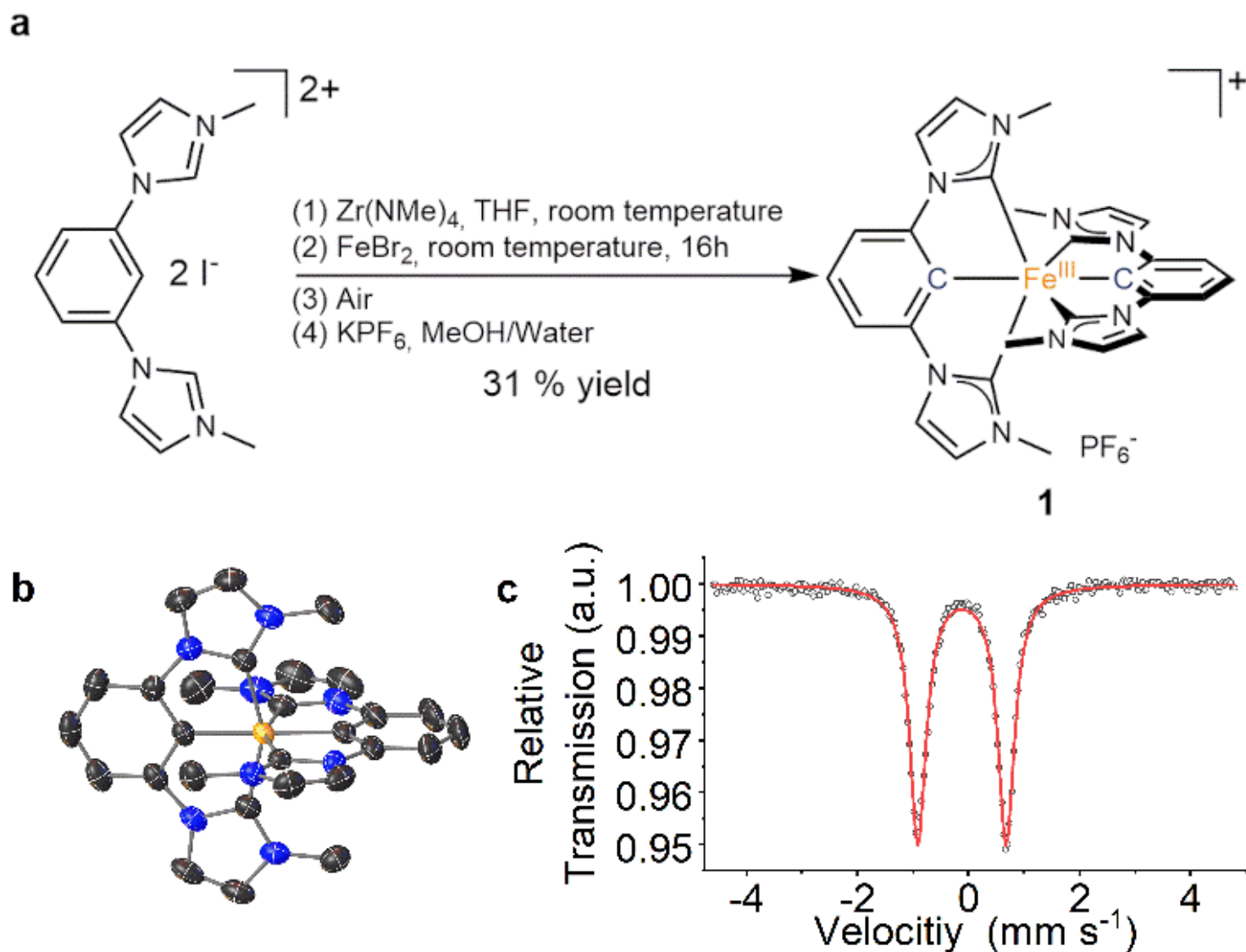


Figure 1

Synthesis, X-ray Structure and Mössbauer Spectrum of $[\text{Fe}(\text{ImP})_2][\text{PF}_6]$. a, Activation of the ligand using a zirconium reagent with subsequent transmetalation onto iron. THF, tetrahydrofuran; MeOH, methanol. Due to the donor strength of the ligand, the complex easily oxidizes under air. b, Crystal structure of $1[\text{PF}_6]$, anisotropic displacement ellipsoids drawn at an electron probability level of 50 %, hydrogen atoms and the $[\text{PF}_6]^-$ anion are omitted for clarity. c, Mössbauer spectrum of $1[\text{PF}_6]$ at 80 K showing the characteristic doublet of a low-spin Fe^{III} complex with $\delta = -0.12 \text{ mm s}^{-1}$ and $\Delta\text{EQ} = 1.59 \text{ mm s}^{-1}$.

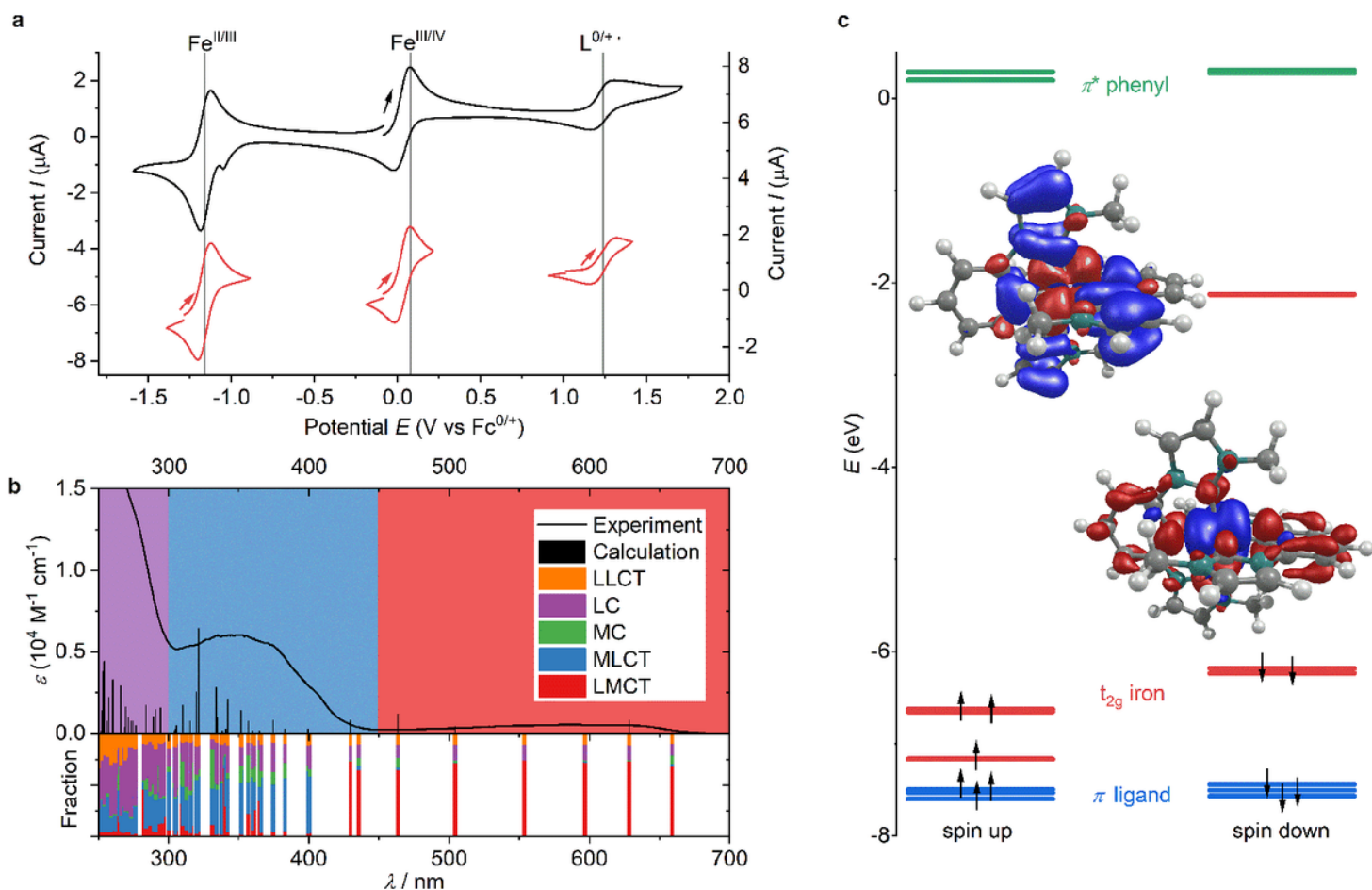


Figure 2

Electrochemical, optical and electronic properties of $[\text{Fe}(\text{ImP})_2][\text{PF}_6]$. a, Cyclic voltammogram of $1[\text{PF}_6]$ (10^{-3} M) in acetonitrile with 0.1 M $[\text{nBu}_4\text{N}][\text{PF}_6]$ as an electrolyte at a scan rate of 100 mV s^{-1} with the full scan in black and the individual waves in red. b, UV-Vis absorption spectrum of $1[\text{PF}_6]$ in MeCN (10^{-5} M) with TDDFT calculated transitions and contributions from intra-ligand charge transfer (LLCT), ligand centered π - π^* (LC), metal-centered (MC), ligand-to-metal charge transfer (LMCT) and metal-to-ligand charge transfer (MLCT) states. c, Molecular orbital scheme showing the highest occupied orbitals (t_{2g} orbitals highlighted red, ligand-based orbitals blue) and the lowest unoccupied orbitals (π^* orbitals of the phenyl moiety highlighted green). The transition densities of the dominant LMCT (above) and MLCT (below) transitions are also depicted here (hole (blue) and electron (red)).

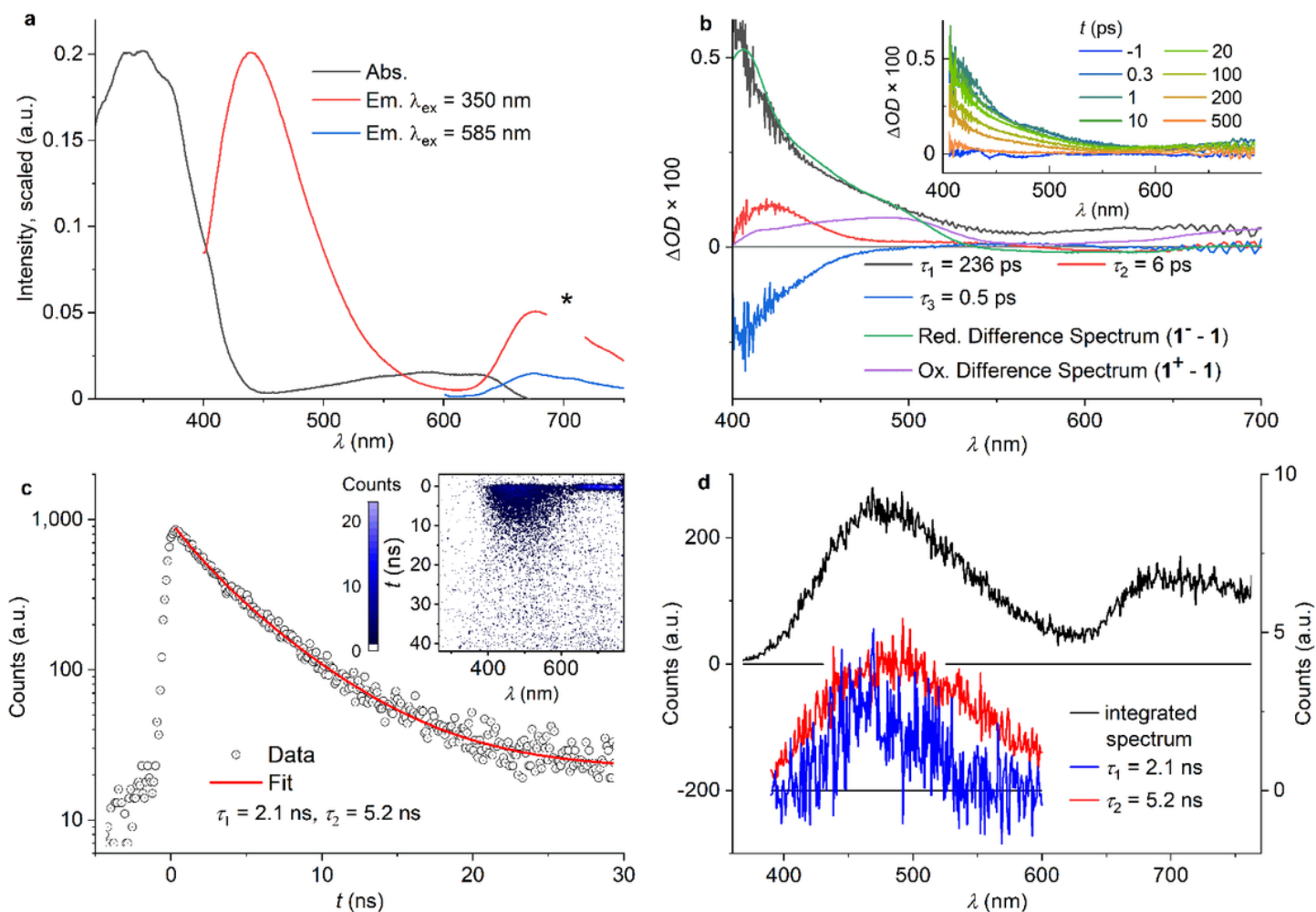


Figure 3

Excited state spectroscopy and characterization of [Fe(ImP)₂][PF₆]. a, Absorption and emission spectra of 1 in CH₃CN at $\lambda_{\text{ex}} = 350$ nm and 585 nm. At 700 nm, the second diffraction order of the excitation light ($2\lambda_{\text{ex}}$) can be observed (*). b, Decay associated amplitude spectra of decay components with $\tau_1 = 236$ ps, $\tau_2 = 6.1$ ps and $\tau_3 = 0.5$ ns obtained from transient absorption (TA) data after excitation at 330 nm and compared to the reduction and oxidation difference spectra extracted from spectro-electrochemical measurements. Inset: TA spectra at the given delay times. c, Decay of the fluorescence between 390 nm and 600 nm obtained from streak camera measurements (inset) of a degassed solution of 1[PF₆] in acetonitrile after 330 nm excitation. It exhibits a double exponential behavior with time constants of 2.1 and 5.2 ns. d, Time-integrated spectrum obtained from streak camera measurements with $\lambda_{\text{ex}} = 330$ nm, showing a close resemblance with the fluorescence spectrum, and the amplitude spectra of the 2.1 ns and the 5.2 ns component.

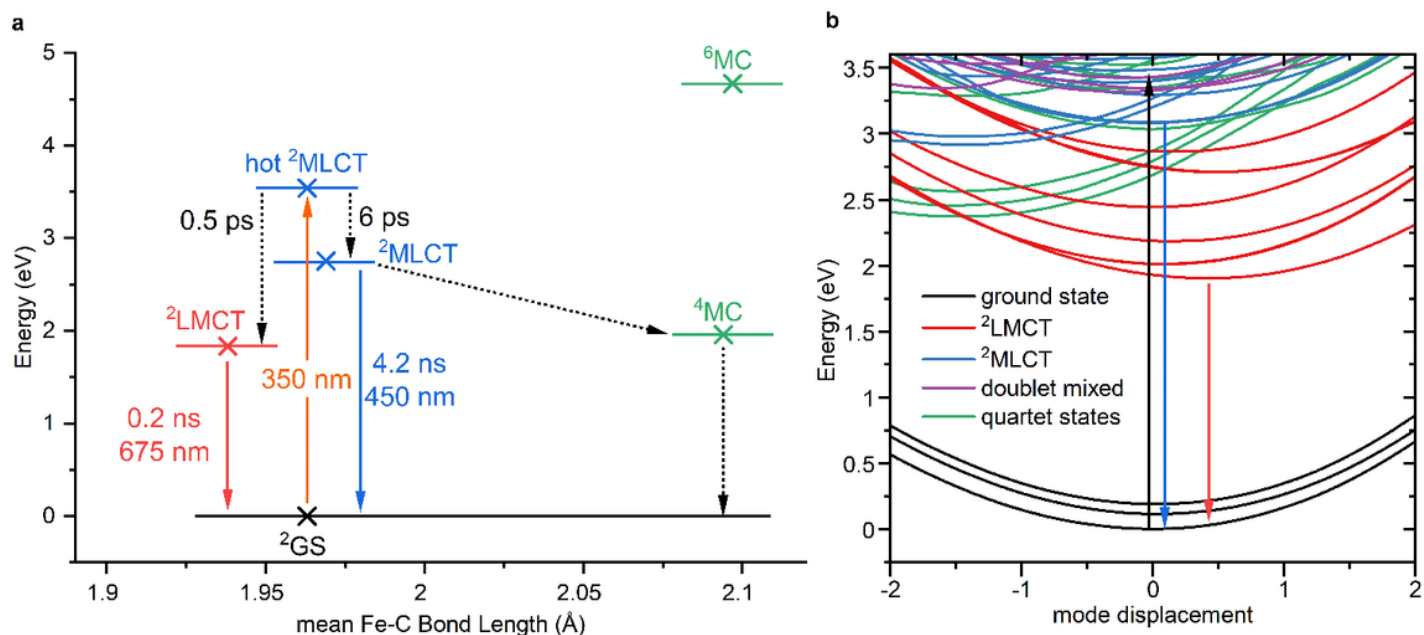


Figure 4

Summary of deactivation pathways and associated time scales of $[Fe(ImP)_2][PF_6]$. a, Jablonski diagram based on the experimental results and calculated ground state DFT energies of the optimized doublet, quartet and sextet states in their respective geometry (crosses). The 2LMCT and 2MLCT geometries are approximated from the calculated FeII and FeIV geometries. The orange arrow indicates the excitation at 350 nm, the dotted arrows radiationless transitions, the blue arrow the MLCT and the red arrow the LMCT emission. b, TDDFT potential energy curves for displacement along the a1 symmetry vibrational mode (in D2d symmetry), showing doublet LMCT, MLCT and mixed LMCT/LC states, as well as quartet MC states. The black arrow indicates the excitation at 350 nm, the blue arrow the MLCT emission and the red arrow the LMCT emission.

Supplementary Files

This is a list of supplementary files associated with this preprint. Click to download.

- [js01690masq.cif](#)
- [DFTcoordinates.pdf](#)
- [js01690masqCheckCif.pdf](#)
- [ExtendedData.docx](#)